Validation of a patient-specific one-dimensional model of the systemic arterial tree

Philippe Reymond,[1] Yvette Bohraus,[1] Fabienne Perren,[2] Francois Lazeyras,[3] and Nikos Stergiopulos[1]

[1]*Laboratory of Hemodynamics and Cardiovascular Technology, Ecole Polytechnique Fédérale de Lausanne, Switzerland; and Departments of* [2]*Clinical Neurosciences, Neurology, and* [3]*Radiology, Geneva University Hospital, University Hospital and Medical faculty of Geneva, Geneva, Switzerland*

Reymond P, Bohraus Y, Perren F, Lazeyras F, Stergiopulos N. Validation of a patient-specific one-dimensional model of the systemic arterial tree. *Am J Physiol Heart Circ Physiol* 301: H1173–H1182, 2011. First published May 27, 2011; doi:10.1152/ajpheart.00821.2010.—The aim of this study is to develop and validate a patient-specific distributed model of the systemic arterial tree. This model is built using geometric and hemodynamic data measured on a specific person and validated with noninvasive measurements of flow and pressure on the same person, providing thus a patient-specific model and validation. The systemic arterial tree geometry was obtained from MR angiographic measurements. A nonlinear viscoelastic constitutive law for the arterial wall is considered. Arterial wall distensibility is based on literature data and adapted to match the wave propagation velocity of the main arteries of the specific subject, which were estimated by pressure waves traveling time. The intimal shear stress is modeled using the Witzig-Womersley theory. Blood pressure is measured using applanation tonometry and flow rate using transcranial ultrasound and phase-contrast-MRI. The model predicts pressure and flow waveforms in good qualitative and quantitative agreement with the in vivo measurements, in terms of wave shape and specific wave features. Comparison with a generic one-dimensional model shows that the patient-specific model better predicts pressure and flow at specific arterial sites. These results obtained let us conclude that a patient-specific one-dimensional model of the arterial tree is able to predict well pressure and flow waveforms in the main systemic circulation, whereas this is not always the case for a generic one-dimensional model.

wave propagation; cerebral circulation; noninvasive measurements techniques; phase-contrast-magnetic resonance imaging; Doppler

AT PRESENT, one-dimensional models are best suited to study flow and pressure waveforms along the whole or extensive parts of the systemic and pulmonary circulation. They can provide insight regarding wave propagation and reflection phenomena and allow for characterization of ventricular-arterial coupling. Because of their relatively low computational cost and complexity, one-dimensional models have been extensively used in the past to study different pathologies, such as hypertension by Westerhof et al. (30, 31), arteriosclerosis by Raines et al. (22), stenoses by many authors (2, 5, 7, 10, 13, 17, 21, 25, 26, 32), anatomical variations of cerebral arteries, arterial occlusion by Alastruey et al. (1), or to study surgery plans by Wan et al. (28). The main characteristics of previous one-dimensional models have been published in a previous article from our laboratory (23).

The primary question addressed in this article was the validity of the generic one-dimensional model predictions. The approach we followed was to compare the predictions of the generic one-dimensional model with the average pressure and flow waveforms measured noninvasively in a group of healthy young individuals. The underlying hypothesis was that although the generic model would not represent precisely a specific individual it should represent reasonably well the average of the group. Hence, the model validation was strictly qualitative. Reymond et al. 2009 (23) suggested that future work should be focused on a quantitative validation of the model on a specific subject with the arterial tree constructed based on geometry and elasticity data derived from measurements on the specific person. The model predictions could then be compared with noninvasive in vivo measurements on the same subject. This is exactly the method followed and reported in the present follow-up study.

METHODS

Physiological data. To build a coherent patient-specific one-dimensional model of the arterial tree, we performed measurements of the arterial geometry using MR angiography on a 30-year-old healthy volunteer (height, 183 cm; weight, 90 kg). Noninvasive pressure and flow measurements were performed on the same volunteer using applanation tonometry (pressure) and Doppler and MRI (flow). All measurements were obtained with the subject at rest in the supine position with the heart rate nearly identical for the different measurements. The averaged heart cycle for all measurement locations was in the range of 0.92–1.05 s for MRI, 0.98–0.99 s for tonometry, and 0.96–1.04 s for Doppler. Measurements were performed at the Geneva University Hospital (HUG), according to a protocol approved by the local ethics committee. The volunteer provided written, informed consent.

The arterial tree model is based on the 103-segment model reported by Reymond et al. (23) with the primary model equations rewritten in the APPENDIX. The present patient-specific arterial tree has been updated by removing the coronary and anterior choroidal arteries, vessels that were not available from the imaging performed in the specific volunteer (Fig. 1). The specific arterial tree has 94 arterial segments, specified by their proximal and distal cross-sectional area and length. The geometrical parameters are given in Table 1.

Angiography. MRI time of flight measurements were carried out on a 3T scanner (Siemens Trio-Tim 3T System). Images of the systemic circulation were obtained by addition of the contrast agent (23 ml OMNISCAN 0.5 mmol/ml + 25 ml NaCl) using adapted sequence parameters [flip angle, 17°; TE = 1.02 ms; TR = 2.6 ms; field of view (FoV), 431 mm × 834 mm; slice thickness, 1.3 mm]. Data on cerebral (flip angle, 15°; TE = 3.69 ms; TR = 22 ms; FoV, 177 mm × 199 mm; slice thickness, 0.6 mm), neck (flip angle, 60°; TE = 5.1 ms; TR = 20 ms; FoV, 160 mm × 200 mm; slice thickness, 1.5 mm), and lower limb circulation (flip angle, 60°; TE = 5.1 ms; TR = 20 ms; FoV, 240 mm × 300 mm; slice thickness, 1.5 mm) were acquired without contrast agent use.

Address for reprint requests and other correspondence: P. Reymond, Lab. of Hemodynamics and Cardiovascular Technology, Ecole Polytechnique Fédérale de Lausanne, EPFL/STI/IBI2/LHTC, AI 1231, Station 15, CH-1015 Lausanne, Switzerland (e-mail: philippe.reymond@epfl.ch).
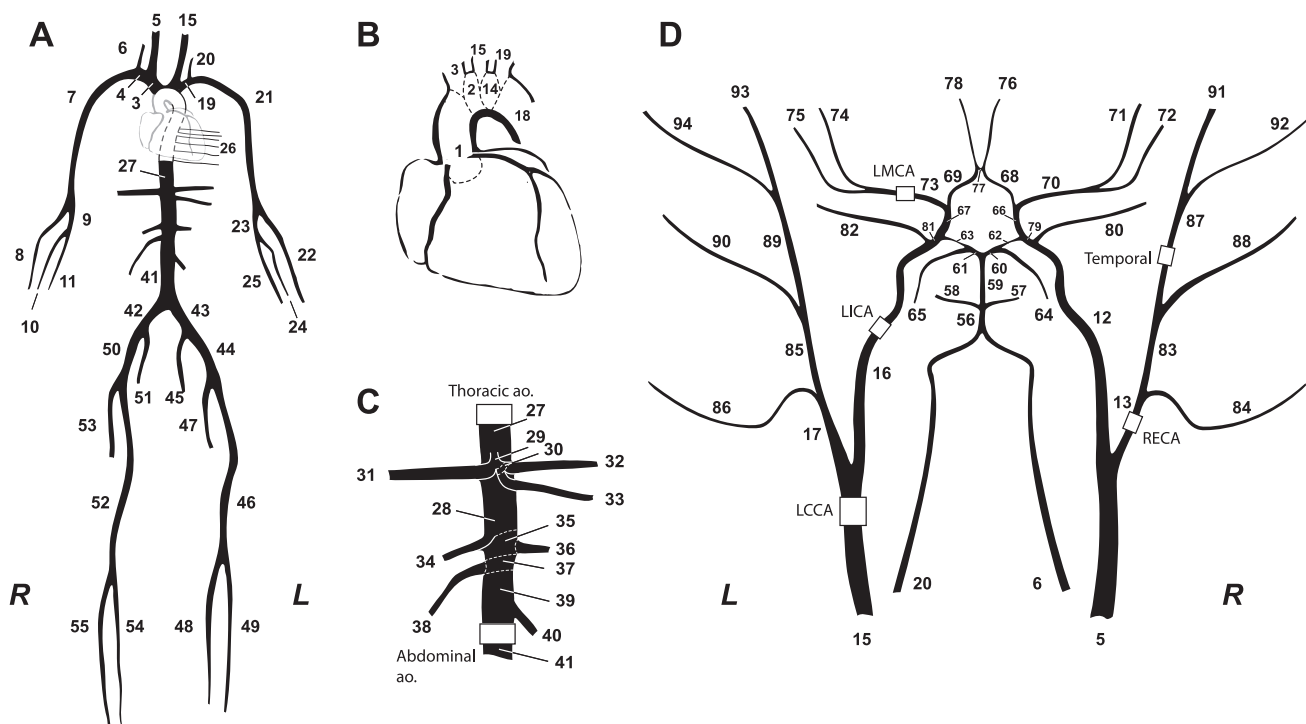
Fig. 1. Schematic representation of the arterial tree adapted from Reymond et al. (23). *A*: main systemic arterial tree. *B*: detail of the aortic (ao.) arch (coronary arteries are not taken into account). *C*: detail of the principal abdominal aorta branches. *D*: schematic of the detailed cerebral arterial tree, which is connected via the carotids (segments 5 and 15) and the vertebrals (segments 6 and 20) to the main arterial tree shown in *A* (anterior choroidal arteries are left out). Locations where in vivo measurements were performed are presented. L, left; R, right; LMCA, left middle cerebral artery; LICA, left internal carotid artery; LCCA, left common carotid artery; RECA, right external carotid artery.

The arterial tree geometry was reconstructed in three dimension (Fig. 2) from MRI magnitude data (ITK Snap software). Dicom images were processed using a gradient diffusion filter. The presegmented vasculature region was computed based on contrast threshold. This region was used as an initial region to obtain a more accurate segmentation using an edge detection method based on contrast intensity gradient.

Geometric measurements for each arterial segment were acquired with ICEM CFD 11 software (ANSYS, Canonsburg, PA). Local diameter values were estimated from the average of four measurements at each cross section, whereas length measurements were assessed along the centerline of the arterial segment (Table 1). Arterial tree dimensions were taken as measured and not adapted to minimize reflection coefficients for forward waves at bifurcations, as was the case previous work from our laboratory (23), where reflection coefficients were limited to 0.1. The effect of such optimization will be elaborated in the discussion.

In Vivo Measurements

Volume flow rate waveforms were obtained in several systemic arteries [common carotid arteries (CCA), ascending, descending, thoracic, and abdominal aorta, iliac, and femoral arteries] using gated phase-contrast (PC)-MRI and in precerebral and cerebral arteries [CCA, external carotid arteries (ECA), internal carotid arteries (ICA), vertebral arteries (VA), and middle cerebral artery (MCA)] using B-mode and color-coded duplex flow imaging. Pressure waveforms were measured at superficial arteries (radial, carotid, and temporal arteries) using applanation tonometry. Mean blood flow rates measured by the PC-MRI and Doppler techniques presented hereafter are summarized in Table 2. The end-diastolic flow waveform foot was set as reference for temporal alignment of cardiac cycles, and 5–15 cycles were averaged to obtain a smoothed waveform.

Blood flow measurement using PC-MRI. Sequences that provided velocity measurements over an entire cardiac cycle at selected cross section locations were performed. Two-dimensional through plane PC-MRI sequences (slice thickness, 6 mm; TE/TR, 3.3/51.7 ms; flip angle, 20°; FoV, 220 × 320 mm; iPat Siemens Parallel Acquisition Technique, VENC; 150 cm/s for the CCA and the thoracic aorta, 110 cm/s for the abdominal aorta) were acquired in resting conditions. The measurement planes were determined using flash angiography images to ensure that the plane was perpendicular to the vessel axis. For aortic measurements, breath-hold sequences were performed over a period of 19 s to minimize movement artifacts. Twenty index finger pulse pressure gated phase and magnitude images were acquired at each measurement location.

Arterial cross sections were automatically segmented (Argus Flow VA60C 2004; Siemens) to follow lumen area changes over the heart cycle. Volume flow rate was the integral of the velocities across the lumen.

Blood flow measurement using color-coded duplex ultrasound. Transcranial color-coded duplex flow imaging (CDFI) with a 5–8 MHz linear phase array and a 2–4 MHz sectorial transducer were used to assess blood flow velocities in the cerebral vasculature (Toshiba medical device, Aplio 80). CDFI was performed at the cervical (CCA, ECA, ICA: extracranial window, insonation angle 60°) and cerebral (VA: suboccipital window, insonation angle 60°; MCA: temporal window, insonation angle 0°) vessels. Blood flow was computed from the peak velocity waveforms using the Witzig-Womersley theory, assuming constant lumen diameter values. Diameters of extracranial arteries were obtained using Doppler M-mode, whereas geometrical dimensions of ICA were determined by MRI angiography.

Pressure measurement using applanation tonometry. Pressure waveforms over 10 heart cycles were acquired at the distal radial artery, distal CCA, and temporal arteries (Fig. 2, *F* and *H*) with

Table 1. *Geometry, distensibility, viscoelastic properties, and peripheral resistances and compliances of the arterial tree*

| Arterial Segment Name	Arterial Segment Number (right/left)	Arterial Segment Length (mm)	Proximal Lumen Diameter (mm)	Distal Lumen Diameter (mm)	Distensibility (Dw) $(10^{-3}$ mmHg$^{-1})$	Viscoelasticity Coefficient (a)	Terminal Resistance $(R_1 + R_2)$ (mmHg s/ml)	Terminal Compliance (C_T) 10-5 (ml/mmHg) (right/left)
Ascending aorta 1	1	55	30.5	28.9	5.49	0.05		
Aortic arch A	2	8	28.3	28	5.32	0.05		
Brachiocephalic	3	46	13.1	12.3	3.3	0.08		
Subclavian A	4/19	23/53	11.8/10	10.8/9.2	3.08/2.79	0.09/0.1		
Common carotid	5/15	94/139	7.8/7.3	7.2/7.1	2.41/2.35	0.11		
Vertebral	6/20	149/148	3.5/3.3	1.7/2.4	1.27/1.35	0.14		
Brachial	7/21	299/333	8/7	3.9/3.8	2.09/1.98	0.12		
Radial	8/22	235	2.6/2.4	2.2/2.0	1.21/1.15	0.14	49.9	198.8/153.7
Ulnar A	9/23	67	2.6/3.0	2.4/2.9	1.25/1.37	0.14		
Interosseous	10/24	79	1.5/1.3	1.3/1.2	0.88/0.81	0.15	99.8	51.4/40.8
Ulnar B	11/25	171	2.3/2.8	2.0/2.5	1.13/1.29	0.14	99.8	153.7/287.9
Internal carotid	12/16	178/177	6.5	4.4	1.99	0.12		
External carotid 1	13/17	55/67	5.6/5.3	5.0/4.9	1.95/1.9	0.12/0.13		
Aortic arch B	14	9	28	27.8	5.29	0.05		
Thoracic aorta A	18	148	27	21.3	4.85	0.05		
Intercostals	26	14	7.5	7	2.36	0.11	10.4	1,959
Thoracic aorta B	27	84	20	19.8	4.32	0.05		
Abdominal aorta A	28	18	20	19.8	4.32	0.05		
Celiac A	29	9	9.3	8.5	2.67	0.1		
Celiac B	30	9	8.5	7.6	2.51	0.11		
Hepatic	31	34	5.5	5.4	1.99	0.12	27.2	2,022
Gastric	32	71	3.2	3	1.42	0.14	40.5	454
Splenic	33	241	6.2	5.3	2.05	0.12	17.4	2,017
Superior mesenteric	34	60	7.6	7.4	2.41	0.11	5.9	4,600
Abdominal aorta B	35	7	19.5	17.5	4.13	0.05		
Renal	38/36	27/46	6.3/5.7	5.5/5.0	2.08/1.96	0.12	7.1	2,200/1,713
Abdominal aorta C	37	7	17.5	17.3	3.99	0.05		
Abdominal aorta D	39	43	17.3	17.2	3.97	0.05		
Inferior mesenteric	40	50	4.7	3.2	1.64	0.13	33.3	586
Abdominal aorta E	41	43	17.8	17.6	4.03	0.05		
Common iliac	42/43	86/85	11.5/12.5	11.4/12.2	3.1/3.25	0.09/0.08		
External iliac	50/44	139/141	11.0/11.3	8.8/11	2.84/3.05	0.1/0.09		
Inner iliac	51/45	30	6.0/8.1	5.5/6.3	2.05/2.35	0.12/0.11	49.9	2,167/3,253
Femoral	52/46	446/444	8.5/8.0	6.9/6.4	2.44/2.35	0.11		
Deep femoral	53/47	55	7.0/6.5	6.7/6.0	2.28/2.16	0.11/0.12	33.3	3,568/2,711
Posterior tibial	54/48	417/410	4.4/4.8	1.8/2.1	1.41/1.51	0.14	79.8	155/227
Anterior tibial	55/49	422/417	3.1/3.2	1.9/2.1	1.24/1.29	0.14	79.8	157/199
Basilar artery 2	56	20	3.4	3.1	1.46	0.32	56	
R superior cerebellar	57/58	15/10	1.7	1.4	0.93	0.33	200	12.8
Basilar artery 1	59	5	2.7	2.5	1.27	0.32		
Posterior cerebral 1	60/61	2	1.6/2.2	1.55/2.15	0.94/1.14	0.33/0.32		
Posterior communicating	62/63	4	1.8/0.9	1.75/0.85	1.01/0.66	0.33		
Posterior cerebral 2	64/65	12	2.3/2.1	1.3/1.9	1.02/1.09	0.33/0.32	80.1	12.1/27.4
Internal carotid distal	66/67	4	3.9	3.8	1.61	0.31		
Anterior cerebral 1	68/69	12/11	1.6/2.5	1.4/2.3	0.92/1.21	0.33/0.32		
Middle cerebral 1	70/73	12/17	3.0/2.8	2.5	1.32/1.29	0.32		
Middle cerebral 2 superior branch	71/74	8	1.1/1.2	1.0	0.74/0.76	0.33	107	5.2/5.3
Middle cerebral 2 inferior branch	72/75	8	2.3/2.2	1.0	0.97/0.95	0.33	107	6.8/6.6
Anterior cerebral 2	76/78	24/23	1.7/1.9	1.2/1.4	0.90/0.97	0.33	80.1	9.0/13.3
Anterior communicating	77	2	1.3	1.25	0.83	0.33		
ICA sinus	79/81	11/10	4.2	4	1.67	0.31		
Ophthalmic	80/82	11/10	1	0.5	0.6	0.33	200	1.06
External carotid 2	83/85	61/60	4.5	3.9/4.0	1.7	0.13		
Superior thyroid ascending pharyngeal lingual facial occipital	84/86	101/100	2.2/2.3	1.1	0.98/0.99	0.15	181	21.5/22.0
Superficial temporal	87/89	61/60	3.6/3.5	3.4/3.3	1.52/1.5	0.14		
Maxillary	88/90	91	2.5/2.43	1.1	1.02	0.15	181	22.3/22.6
Superficial temporal frontal branch	91/93	100/102	2.5	1.6	1.09/1.1	0.14	181	46.9/48.0
R superficial temporal parietal branch	92/94	101/103	2.5	1.6	1.09/1.1	0.14	181	46.9/48.0

ICA, internal carotid arteries.
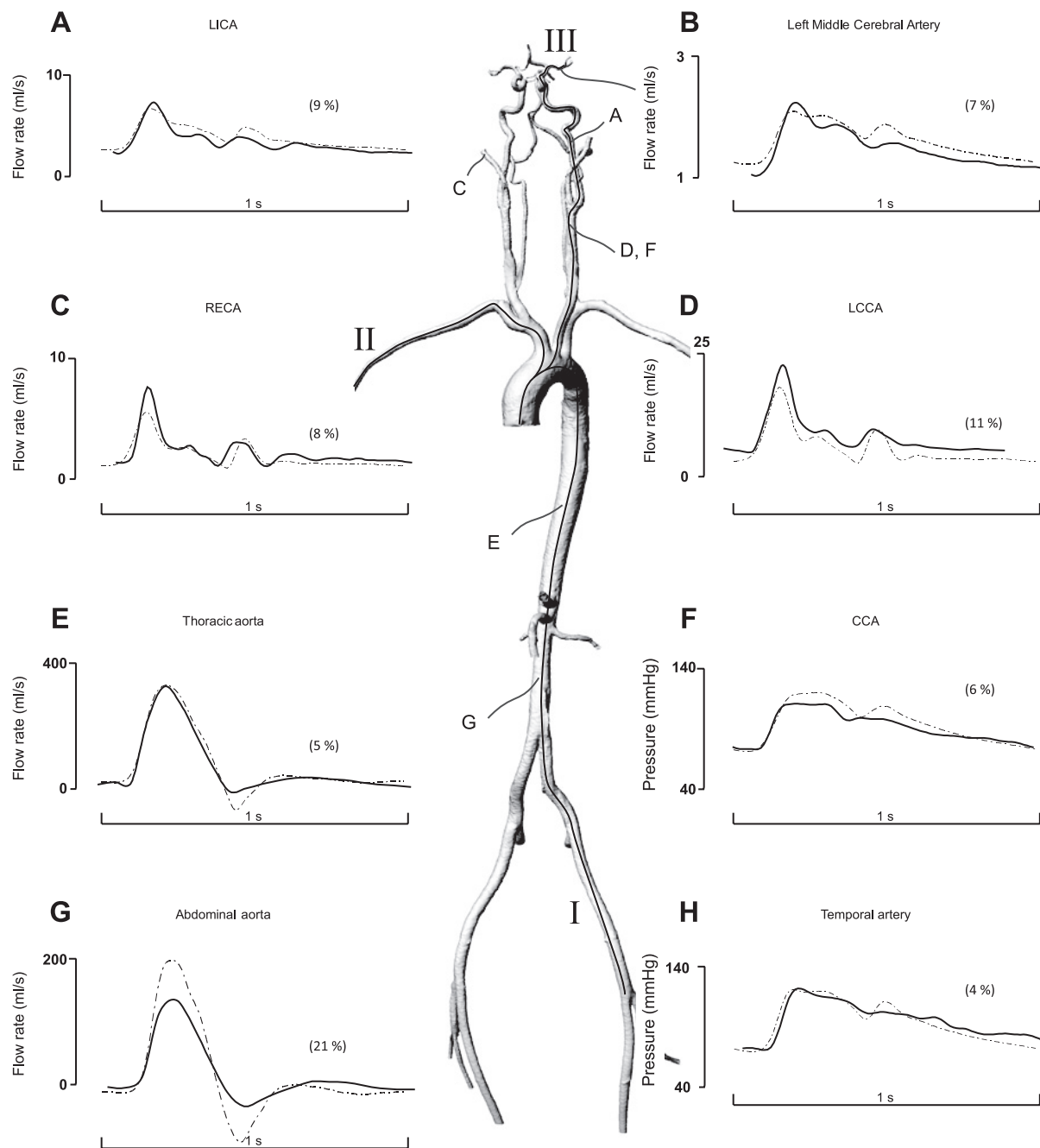
Fig. 2. Model predictions (dash dot) compared with in vivo measurements of flow and pressure waves (continuous line) for different systemic and cerebral arteries. Flow is measured with B-mode color-coded duplex flow imaging technique in the LICA (*A*), LMCA (*B*), and RECA (*C*), with phase-contrast (PC)-MRI in the LCCA (*D*) in the thoracic aorta (*E*) and in the abdominal aorta (*G*). Pressure was measured with applanation tonometry in the common carotid artery (CCA; *F*) and superficial temporal artery (*H*). The central picture is the representation of the 3-dimensional geometry of the patient-specific arterial tree from MRI angiography. In parenthesis are root mean square of the error (RMSE) computed between simulations and measurements and expressed in percentage relative to the in vivo systolic values. Centerlines originate from the ascending aorta, toward the lower limb arteries (I), the right radial artery (II), and the LMCA (III).

applanation tonometry (Millar Instruments, SPT 301, Houston, TX). Brachial sphygmomanometer measurements were taken to calibrate applanation tonometry measurements, assuming that mean and diastolic pressures do not vary much between the brachial, carotid, radial, and temporal locations. Mean sphygmomanometer pressure was calculated as $P_{mean} \cong P_{diastole} + 1/3\ PP$ (24), where PP is the pulse pressure ($P_{sys} - P_{dia}$).

Arterial stiffness assessment. To render the elastic properties of the patient-specific one-dimensional model, we measured the timing of the foot of the pressure wave at the CCA, radial, and temporal artery.

Pressures were measured using applanation tonometry and were combined with simultaneous measurements of ECG (PSYLAB Contact Precision Instruments, Boston, MA). The time delay between the foot of the pressure wave and the ECG R-wave was 178, 96, and 104 ms for the radial, the distal part of common carotid, and the temporal arteries, respectively. Distensibilities of all vessels of the one-dimensional model were then adjusted by a common factor to obtain the minimum difference between the simulated and measured travel times. Local distensibility was taken to be a function of the transmural pressure and lumen diameter (Appendix Eq. A3–A7).

Table 2. *Mean blood flow rate for different central and cerebral arteries from our in vivo measurements (phase-contrast MRI and Doppler ultrasound) as well as the values obtained from the one-dimensional model*

Artery	Phase-contrast MRI (ml/s)	Ultrasound (ml/s)	Model (ml/s)
Aorta			
Ascending	103		103.1
Descending	72		82.8
Thoracic	70		73.0
Abdominal	17		15.4
External iliac artery			
Right	7.3		5.5
Left	5.3		5.6
CCA			
Right	9.7	7.0	6.0
Left	8.1	5.6	6.0
ICA			
Right		4.7	4.1
Left		3.9	4.1
ECA			
Right		2.8	1.9
Left		2.5	1.9
Vertebral arteries			
Right		1.3	0.4
Left		1.3	0.9
MCA			
Right		1.7	1.8
Left		1.4	1.8

CCA, common carotid artery; ECA, external carotid arteries; MCA, middle cerebral artery.

Mathematical Description of the Model

The one-dimensional form of the fluid mechanics equations is mentioned in the APPENDIX. The intimal shear stress and nonlinear convective acceleration terms are modeled using the Witzig-Womersley theory. In contrast with our previous work, at the aortic root we impose flow measured in the subject by MRI.

Viscoelastic properties of the arterial wall. The nonlinear viscoelastic constitutive law for the arterial wall, proposed by Holenstein et al. (11) and adapted by Reymond et al. (23), was used in the present study (Eq. A8-A10). Having limited information and testing methods to adjust the viscoelastic coefficients to the specific subject, we used the same model as for the generic tree. However, the viscous coefficients depend on local vessel size (Eq. A.10) and are thus different than the generic tree.

Distal vasculature models at termination sites. All distal vessels are terminated with three-element Windkessel models to account for the proximal and distal resistance and compliance of the distal vascular beds. Distal resistances were adapted to obtain a flow distribution that was close to the flow deduced from the reported mean flow values in Table 2.

Patient-Specific Versus Generic Arterial Tree Model Comparison

To verify the advantages of using a patient-specific arterial tree, we compare the predictions of the patient-specific model with the generic one developed earlier by Reymond et al. (23). We apply the same inflow waveform at the aortic root with the distal Windkessel model values unchanged from the generic model. Global distensibility and systemic vascular resistance of the generic arterial tree is adapted to yield the same central mean and pulse pressure and mean pressure as the patient-specific model. The predictions of the patient-specific and generic arterial tree model are compared with flow measured at the thoracic aorta and ICA and pressure at the superficial temporal artery. A quantitative assessment of the relative error is performed by computing the root mean square of the error (RMSE) of the predicted waveforms compared with the in vivo measurements. RMSE is considered to be a good indicator of the error, but, is not the best index to qualify the reproduction of specific wave features.

RESULTS

Patient-Specific Arterial Tree Model Predictions Versus In Vivo Measurements

Figure 2 shows a comparison of predicted pressure and flow waveforms with measured waves at different arterial locations. The predicted flow waves in the main aortic segments (thoracic and abdominal aorta, Fig. 2, *E* and *G*) and CCA (Fig. 2*D*) are compared with PC-MRI measurements. The predicted flow waveform at the ICA (Fig. 2*A*), at the MCA (Fig. 2*B*), and ECA (Fig. 2*C*) is compared with ultrasound measurements. Pressure waveforms measured with applanation tonometry are compared with model predictions in the CCA (Fig. 2*F*) and the superficial temporal artery (Fig. 2*H*). We observe that the overall agreement in both amplitude and wave shape features, at all arterial locations and for both pressure and flow, is good. The relative RMSE for pressure is below 10%, with 4%, 6%, and 6% at the temporal, CCA, and radial artery, respectively. Relative RMSE for flow is also below 10%, except at the left CCA and abdominal aorta, where RMSE is 11% and 21%, respectively (Table 3). The error at the abdominal aorta was due to a marked difference in local flow pulsatility.

Patient-Specific Versus Generic Arterial Tree Model Comparison

The predictions of the patient-specific model are compared with those of the generic one in Fig. 3. We observed that, overall, the patient-specific model reproduces the features of the flow and pressure waves better in terms of both amplitude and wave shape. The RMSE values of the patient-specific model predictions are summarized in Table 3. These RMSE values are lower than for those obtained from the same locations in the generic model except for the abdominal aorta.

Table 3. *Flow and pressure root mean square of the error are computed between model simulations and in vivo measurements*

Arteries	Flow					Pressure			
	Left ICA	Left MCA	Right ECA	Left CCA	Thoracic Aorta	Abdominal Aorta	Temporal	CCA	Radial
Arteries, %									
Patient specific	9	7	8	11	5	21	4	6	6
Generic	12	12	15	14	13	18	5	11	13

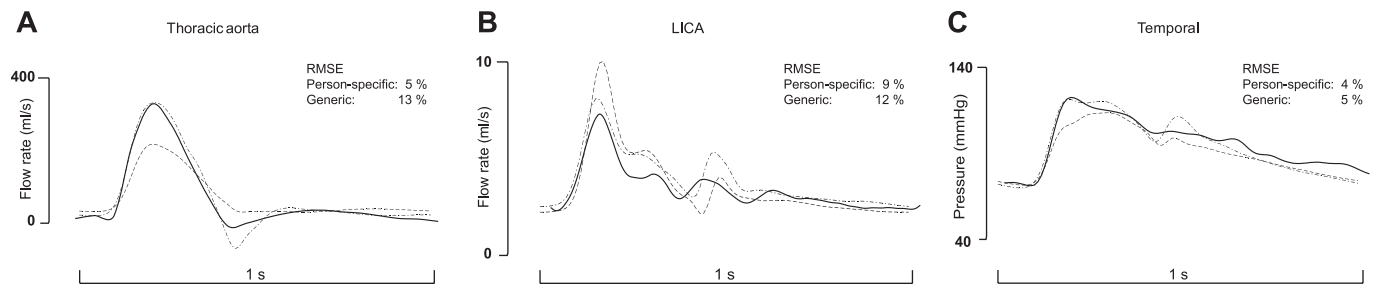Values are expressed in percentage relative to the in vivo systolic values.

Fig. 3. Generic (dash) and specific (dash dot) arterial tree model predictions are compared with in vivo measurements (continuous line) of flow and pressure waves for different systemic and cerebral arteries. Flow is measured with PC-MRI in the thoracic aorta (*A*) and with color-coded duplex ultrasound in the LICA (*B*). Pressure was measured with applanation tonometry in the superficial temporal artery (*C*).

DISCUSSION

Patient-Specific Arterial Tree

Flow in cerebral and precerebral arteries. Flow rate waveforms in cerebral and carotid arteries are well reproduced, the early and late systolic peaks are present, and their relative amplitudes are predicted accurately. In the case of the left MCA, the pulsatility of the predicted wave is less pronounced (Fig. 2*B*). At the right ECA level, all wave features are well reproduced with the wave peaks present at the correct time. However, the early systolic peak amplitude is underestimated by the model compared with the in vivo measurements (Fig. 2*C*). The flow waveform features for the left CCA are similar, whereas the average flow is different. Mean flows from the in vivo measurements were used to derive the distal resistances of the Windkessel models. However, distal anastomoses affect the flow distribution among the different branches feeding the Circle of Willis.

Flow in the central aorta. Thoracic aorta flow waveform is discussed hereafter when specific and generic arterial tree are compared. Concerning the abdominal aorta, systolic peak and dicrotic notch have the same relative timing in the model and in the measurements, but their amplitudes differ. Mean flow values for the one-dimensional model prediction and PC-MRI measurements also differ [15.4 vs. 17 (ml/s), respectively], but this difference may not entirely explain the large discrepancy in pulsatility. We recognize that wave reflection phenomena that require a precise geometry of the distal vessels was not properly reproduced by the patient-specific model. Error in PC-MRI measurements may also contribute to the differences in pulsatility, e.g., error in the location and segmentation of the aortic cross section.

Pressure in superficial arteries. Concerning the CCA, the patient-specific model and applanation tonometry present a kind of plateau during systole that is marked by the presence of early and late systolic peaks. There is a time shift between the dicrotic notch in the patient-specific model and measured waveforms that is discussed in more detail hereafter. In the distal superficial temporal artery, the waves present a distinctive separation of the two peaks with the early systolic peak elevated. The comparison between the model and experimental waves is very favorable.

Model of the left ventricle. In our previous work, we implemented a simple model for the left ventricle based on the varying elastance model. In the present study, we preferred to use the flow waveform measured at the aortic root for the proximal boundary condition. This decision was motivated by the fact that the patient-specific and the generic model are different and in consequence they would represent different afterloads to the heart, yielding different flows in the proximal aorta.

Patient-Specific Versus Generic Arterial Tree Comparison

Arterial tree geometry. The geometry of the generic model was based on the original Noordergraaf arterial tree (19), later adapted by Westerhof et al. (31) and by Stergiopulos et al. (25). A detailed description of the cerebral circulation was added from averaged literature geometric data and completed by real patient scans.

As seen in Fig. 4, the lumen areas of the patient-specific tree are consistently higher than the corresponding values of the generic tree. Differences can be as large as 55% lumen diameter (distal segment of the thoracic aorta) or as small as 5% at ascending aorta. Overall, the differences are quite nonhomogeneously distributed and this points toward the fact that each arterial tree has its own geometrical profile and, inconsequence, its own wave transmission and reflection profile.

Flow in the aorta. Figure 3 shows that the patient-specific model closely reproduces the systolic part of the thoracic aorta flow waveform. In contrast, the generic model underestimates it greatly, despite the fact that the wave shape predicted by the generic model is acceptable and mean flow in both models were nearly identical (~73 ml/s). We observe that the dicrotic notch predicted by the specific model at the thoracic and abdominal aorta is more pronounced than that measured by PC-MRI and obtained by the generic arterial tree (Fig. 3*A*).

This may be attributed to augmented wave reflection phenomena in the specific arterial tree. In Fig. 4 we plotted the lumen area and local reflection coefficients of the specific and generic model along the main aortic trunk and the iliac arteries. We observe that the specific arterial tree presents higher reflection coefficient at the iliac bifurcation (0.1) and, more importantly, values up to 0.3 (not visible in this figure) in the distal bifurcations, the femoral and tibia regions. We have chosen to keep the geometry as measured and not interfere in the construction of the specific arterial tree by means of optimizing wave reflections. In the generic arterial tree, reflection coefficients were limited to the somewhat arbitrary value of 0.1 by iteratively adjusting the area of downstream vessels. In addition, construction of the arterial tree in the lower limb regions from MRI scans was difficult in comparison with the aortic and cerebral regions. The MRI angiography images obtained for the lower limbs, such as the tibia, presented artifacts and were consequently difficult to segment and obtain
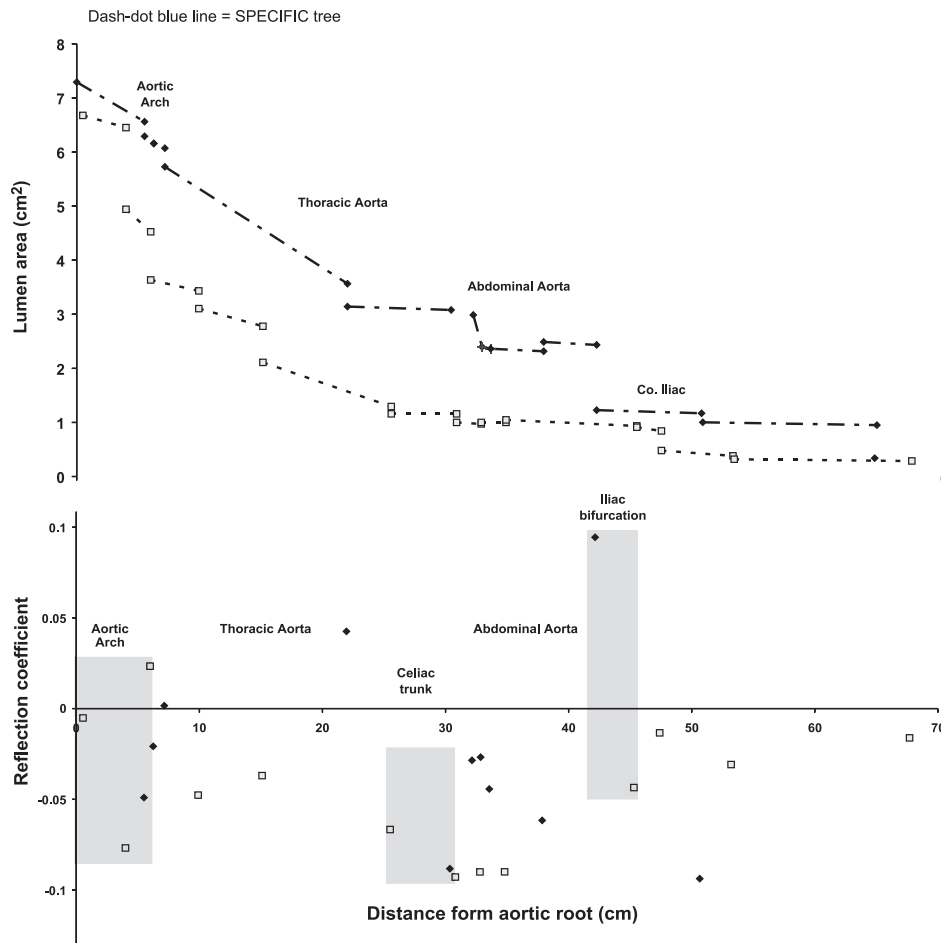
Fig. 4. Lumen area (*top*) and forward wave reflection coefficients (*bottom*) along the aortic root and lower limb arteries. Generic (dash and square marker) and specific (dash dot and diamond marker) arterial tree models are represented. Co. iliac, common iliac.

a precise geometry. These remarks probably explain the higher flow RMSE of the patient-specific model only encountered at the abdominal aorta location (Table 3).

To check whether optimization of reflections in the lower aorta and limbs is of importance, the patient-specific arterial tree was adapted to limit the reflection coefficients at specific locations to a value below 0.1. To achieve this, the area or compliance of the daughter branches can be modified. To avoid affecting the geometry, we adjusted the distensibility either increasing or decreasing its value in the downstream vessels. The dicrotic notch of the predicted flow waveforms was reduced and approached that measured in vivo.

Flow in the ICA. The two first systolic peaks are reproduced well by the specific and generic arterial tree model (Fig. 3*B*). However, the amplitude and pulsatility is better predicted by the patient-specific model. There is still a shift in the phase of the dicrotic notch and the third peak, for both models compared with the measurements. This may be a result of error in the estimation of distal cerebral vessel distensibility using the generic relationship in our models.

Pressure in the temporal superficial artery. Even though the quantitative comparison of specific and generic arterial tree is not as clearly in favor of the specific tree as it is for the flow comparison in the thoracic and internal carotid, the specific model was still able to better reproduce certain key wave features, such as the existence of a pronounced early systolic peak, which was totally missed by the generic model (Fig. 3*C*).

Perspectives on the use of a patient-specific one-dimensional model of the arterial circulation. Our previous work indicated that a generic one-dimensional model can be used to represent systemic arterial flow and pressure in an average young healthy adult and thus can be used to model the average of a population of a given group. In the present work, we have demonstrated that a carefully constructed patient-specific one-dimensional model of the arterial circulation gives substantially better results that a generic one. Earlier studies have also shown that a patient-specific model of the systemic circulation can give good predictions of arterial waves as in Olufsen et al. (20), although the study by Olufsen et al. restricted the comparison of flow waves to the main arteries of the arterial tree and did not include comparison of pressure waves or comparison in arteries of the cerebral circulation. A well-tuned patient-specific model can become a very useful research tool. One can use such a validated model on a specific individual to study a number of important hemodynamic phenomena and validate model predictions with appropriate noninvasive measurements. However, such a patient-specific model requires a large amount of specific data related to geometry, elastic properties, and peripheral impedances of the arterial tree, which would render the applicability of the model, for clinical and even for research purposes, very cumbersome. It is therefore logical to seek other ways to personalize to some extend the generic arterial tree based on fewer and clinically feasible measurements. One such approach would be to use global descriptors

related to the geometry and properties of the arterial tree, which are easily measured, such as body size (height, weight), age, sex, and pulse wave velocity (PWV; i.e., carotid-to-femoral wave speed). One can then scale the geometry of the generic arterial tree based on body size and do similar adjustment on the elastic properties based on PWV. Sex and age can also be taken into account in a statistical manner, as was done previously for the generalized transfer function (6, 12, 29). This approach, which can be refined by adding other noninvasively measured appropriate indicators, has merit to be tested carefully in the future. It could provide a better means for modeling the arterial tree accurately enough without the complexity of a true patient-specific model.

Limitations. Venous circulation, as well as pulmonary circulation, is not included in the patient-specific and generic model. Cerebrospinal fluid pulsation effects on the intracranial arteries are not taken into account, while a mean transmural pressure from the CSF acting on the intracranial vessels (i.e., intracranial pressure) is taken into account.

Even though geometry, flow, and pressure measurements were all performed on the same individual, there are still data (terminal compliance and resistances of the distal Windkessel models) that were not completely patient specific. The peripheral resistances have been set as close as possible to those determined with the patient-specific flow measurements (Table 2). Distal compliances were assumed to be proportional to the area compliance of the last arterial segment, as was done in Ref. 23, since direct measurements are difficult to implement and their effects are shown to be of secondary importance.

We have not performed a detailed sensitivity analysis because of the large parameter space involved. If one looks only at the global parameters of the model, previous studies have assessed this issue. For example, Stettler et al. (26, 27) provide a sensitivity analysis type of table, with the effects of changes in global arterial tree parameters. This work was performed on a one-dimensional tree model similar to ours and thus the validity of their results should apply to our model as well.

In summary, we have constructed, to the best of our knowledge, the first, rather complete, patient-specific one-dimensional model of a human arterial tree. The model accurately predicts pressure and flow waves in the central and peripheral arteries. The patient-specific model compared favorably against a generic one-dimensional model, indicating the importance of knowing well the exact geometry and elastic and resistive properties of the arterial tree.

Conclusions

A patient-specific one-dimensional model of the main systemic circulation, based on specific geometric arterial tree, has been developed. It predicts pressure and flow waveforms shape and wave features at primary systemic circulation locations with a high qualitative agreement compared with in vivo measurements. Quantitative aspects of pressure and flow waveforms are also well reproduced, thereby validating the suitability of the one-dimensional model to predict pressure and flow waves in the entire systemic arterial tree.

APPENDIX: MATHEMATICAL MODEL

The main equations utilized to build the one-dimensional model in Reymond et al. (23) are rewritten hereafter.

Governing Equations

Arteries are considered as straight long tapered segments with viscoelastic walls. The one-dimensional continuity and momentum equations are obtained by integrating the continuity and longitudinal momentum equations of the Navier-Stokes equations:

$$\frac{\partial A}{\partial t} + \frac{\partial Q}{\partial x} = 0 \qquad (A1)$$

$$\frac{\partial Q}{\partial t} + \frac{\partial}{\partial x}\left(\int_A u^2 dA\right) = -\frac{A}{\rho}\frac{\partial P}{\partial x} - 2\pi R\frac{\mu}{\rho}\frac{\partial u}{\partial r}\bigg|_{r=R} + A b_x \qquad (A2)$$

where $A(x,t)$ is the instantaneous arterial lumen area of radius $R(x,t)$, $u(r,x,t)$ is the longitudinal velocity component, $Q(x,t)$ is the volumetric flow rate, and $P(x,t)$ is the transmural pressure. Blood is assumed to be a Newtonian fluid with density, ρ, and dynamic viscosity, μ.

Viscoelastic Properties of the Arterial Wall

The arterial wall behavior is nonlinear and viscoelastic. We assumed that the arterial lumen area at a given location is the sum of a nonlinear elastic, A^e, and viscoelastic, A^v, component, respectively.

$$A(t) = A^e(P(t)) + A^v(t) \qquad (A3)$$

The elastic component of the local area A^e is related to the instantaneous distending pressure, P, via the local area compliance, $C_A^e = \delta A^e/\delta P$. The latter is a function of distending pressure and location. To account for both pressure and location dependence, we assumed that area compliance is the product of a pressure-dependent function, $C_p^e(p)$, and a location-dependant function, $C_d^e(\bar{d},P_{ref})$, such that

$$C_A^e(\bar{d}, P) = C_d^e(\bar{d}, P_{ref}) \cdot C_p^e(P) \qquad (A4)$$

where $C_d^e(\bar{d}, P_{ref})$ gives the compliance for a given local mean lumen diameter, $\bar{d}$, and at a given reference pressure value. The pressure dependency of the compliance in thoracic and abdominal aorta was determined by Langewouters (14). We adapted it to have a normalized and dimensionless function of compliance $C_p^e(P)$, which is equal to 1 at reference pressure and which describes the pressure dependence of compliance,

$$C_p^e(P) = a_1 + \frac{b_1}{1 + \left[\dfrac{P - P_{maxC}}{P_{width}}\right]^2} \qquad (A5)$$

with $a_1 = 0.4\ (-)$, $b_1 = 5\ (-)$, $P_{maxC} = 20$ (mmHg), $P_{width} = 30$ (mmHg) for the entire arterial tree, assuming that the functional dependence of local area compliance on pressure is approximately the same at all arterial locations. Most published data in the literature provide for estimates of local PWV rather than compliance. We therefore derived the values of compliance at reference pressure from PWV values using the relation:

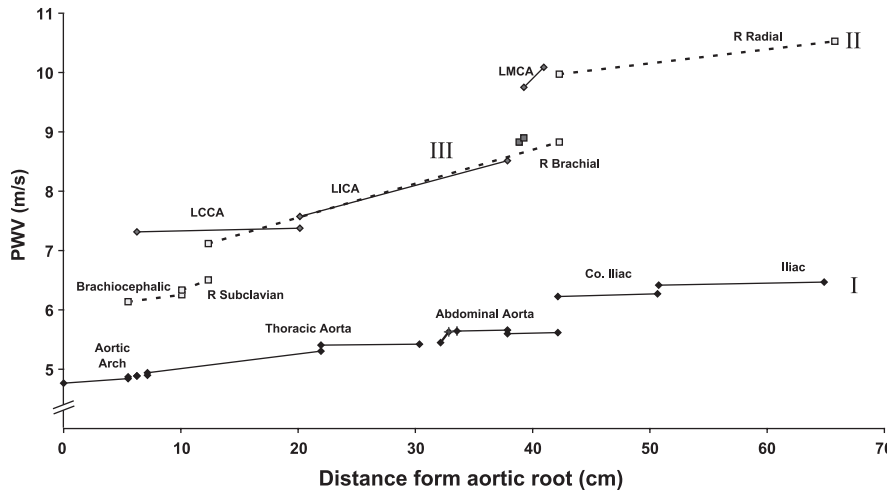$$C_d^e(\bar{d}, P_{ref}) = \frac{A}{\rho PWV^2(\bar{d}, P_{ref})} \qquad (A6)$$

Fig. 5. Pulse wave velocity (PWV) function of the distance from aortic root is presented along 3 center-lines (Fig. 2). Centerlines originate from the ascending aorta, toward the lower limb arteries (I), the right radial artery (II), and the LMCA (III).

Values of PWV reported in the literature (3, 8, 9, 15, 16, 18) for different arteries as a function of the mean arterial lumen diameter were presented. There was a general trend of an inverse global relation between artery size and PWV. To that effect, we fitted an empirical inverse power curve:

$$PWV(\overline{d}, P_{ref}) \approx \frac{a_2}{\overline{d}^{b_2}(P_{ref})} \qquad (A7)$$

The coefficients obtained from the best fit were $a_2 = 13.3$, $b_2 = 0.3$, with $R^2 = 0.6$. PWV computed with Eq. A7 for the patient-specific arterial tree is presented in Fig. 5 along different arterial segments.

To include the viscoelastic component, the model developed by Holenstein et al. (11) was implemented. The viscoelastic behavior was given by the convolution product between the elastic area, A^e, and the derivative of a creep function $J(t)$.

$$A^v(t) = \int_0^\infty \dot{J}(\tau)A^e(P(t-\tau))d\tau \qquad (A8)$$

$$\dot{J}(t) = \tilde{a}\frac{e^{-t/\tau_2} - e^{-t/\tau_1}}{t} \qquad (A9)$$

In Holenstein et al. (11) the values $\tau_1 \cong 0.00081s$, $\tau_2 \cong 0.41s$ were derived from the published data by Bergel (4). According to Holenstein et al. (11), due to the rapid decay of $\dot{J}(t)$, a numerical integration limit, of the duration of half the heart cycle, is enough without any significant loss of accuracy.

Furthermore, based on Bergel's (4) data for the thoracic aorta, abdominal aorta, and femoral artery, we assumed that the viscoelastic coefficient, $\tilde{a}$, increased linearly as the diameter decreased from the heart to the periphery given by

$$\tilde{a} \cong a_3 \cdot \overline{d} + b_3 \qquad (A10)$$

where the linear viscoelastic coefficient, $\tilde{a}$, was obtained by fitting (Eq. A10) on the viscoelasticity data reported by Bergel (4) and Holenstein et al. (11). The best-fit yielded $a_3 = -0.0062$ (mm^{-1}) and $b_3 = 0.16$ (−) ($R^2 = 0.90$) (Fig. 6). For cerebral arteries, which present a much stronger viscoelastic component [Bergel et al. (4)], we assumed the same slope (a_3) as for the other arteries; however, the parameter b_3 was taken as $b_3 = 0.34$ (−) to match the carotid viscoelasticity value.

Distal Vasculature Models and Boundary Conditions at Termination Sites

Peripheral arterial segments are terminated with a 3-element Windkessel (WK3) model, which accounts for the cumulative effects of all distal vessels (small arteries, arterioles, and capillaries) beyond a terminal site. The WK3 model accounts for the proximal resistance (R_1), compliance (C_T), and distal resistance (R_2) of the vascular bed. The relation between pressure and flow in the time domain constitutes the distal boundary conditions and is expressed in differential form as:

$$\frac{\partial Q}{\partial t} = \frac{1}{R_1}\frac{\partial P}{\partial t} + \frac{P}{R_1 R_2 C_T} - \left(1 + \frac{R_1}{R_2}\right)\frac{Q}{R_1 C_T} \qquad (A11)$$

Total peripheral resistances $R_T = R_1 + R_2$ are estimated based on measured mean flow distribution. To define the values of the proximal (R_1) and distal (R_2) resistances, we assumed that the wave reflections at terminal sites vanish at high frequencies. A reflection coefficient at the distal interface is defined as

$$\Gamma(f) = \frac{Z_T(f) - Z_C}{Z_T(f) + Z_C} \qquad (A12)$$

where $Z_C = \rho \cdot PWV/A$ is the characteristic impedance of the last arterial segment proximal to the terminal WK3. Reflections
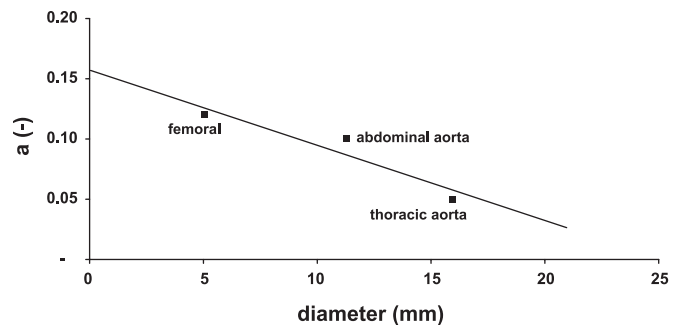

Fig. 6. The creep function coefficient, $\tilde{a}$, function of the mean lumen diameter is presented for 3 locations. These values represent the viscoelasticity component of the arterial wall behavior and were computed from data reported in Refs. 4 and 11.

at high frequencies vanish when $Z_C = Z_T$. At high frequencies, the modulus of the WK3 tends toward a value equal to its proximal resistance ($Z_T = R_1$). Hence, the condition for minimal reflection at high frequencies is $R_1 = Z_C$. Distal resistance is then obtained as $R_2 = R_T - R_1$. To respect the continuity in elastic properties of the terminal vessels, the Windkessel compliance, C_T^i, is assumed to be proportional to the area compliance, C_A^i, of the terminal vessel at its distal end:

$$C_T^i \cong C_T \frac{C_A^i}{\sum C_A^i} \qquad (A13)$$

where $C_T = \Sigma_i \, C_T^i$ is the part of the total volume compliance attributed to peripheral vessels beyond the termination sites.

GRANTS

DISCLOSURES

No conflicts of interest, financial or otherwise, are declared by the author(s).

REFERENCES

1. **Alastruey J, Parker KH, Peiro J, Byrd SM, Sherwin SJ.** Modelling the circle of Willis to assess the effects of anatomical variations and occlusions on cerebral flows. *J Biomech* 40: 1794–1805, 2007.
2. **Avolio AP.** Multi-branched model of the human arterial system. *Med Biol Eng Comput* 18: 709–718, 1980.
3. **Baguet JP, Kingwell BA, Dart AL, Shaw J, Ferrier KE, Jennings GL.** Analysis of the regional pulse wave velocity by Doppler: methodology and reproducibility. *J Hum Hypertens* 17: 407–412, 2003.
4. **Bergel DH.** The dynamic elastic properties of the arterial wall. *J Physiol* 156: 458–469, 1961.
5. **Cassot F, Zagzoule M, Marc-Vergnes JP.** Hemodynamic role of the circle of Willis in stenoses of internal carotid arteries. An analytical solution of a linear model. *J Biomech* 33: 395–405, 2000.
6. **Chen CH, Nevo E, Fetics B, Pak PH, Yin FC, Maughan WL, Kass DA.** Estimation of central aortic pressure waveform by mathematical transformation of radial tonometry pressure. Validation of generalized transfer function. *Circulation* 95: 1827–1836, 1997.
7. **Fitchett DH.** LV-arterial coupling: interactive model to predict effect of wave reflections on LV energetics. *Am J Physiol Heart Circ Physiol* 261: H1026–H1033, 1991.
8. **Giller CA, Aaslid R.** Estimates of pulse wave velocity and measurement of pulse transit time in the human cerebral circulation. *Ultrasound Med Biol* 20: 101–105, 1994.
9. **Hayashi K, Nagasawa S, Naruo Y, Okumura A, Moritake K, Handa H.** Mechanical properties of human cerebral arteries. *Biorheology* 17: 211–218, 1980.
10. **Hillen B, Hoogstraten HW, Post L.** A mathematical model of the flow in the circle of Willis. *J Biomech* 19: 187–194, 1986.
11. **Holenstein R, Niederer P, Anliker M.** A viscoelastic model for use in predicting arterial pulse waves. *J Biomech Eng* 102: 318–325, 1980.
12. **Karamanoglu M, O'Rourke MF, Avolio AP, Kelly RP.** An analysis of the relationship between central aortic and peripheral upper limb pressure waves in man. *Eur Heart J* 14: 160–167, 1993.
13. **Kufahl RH, Clark ME.** A circle of Willis simulation using distensible vessels and pulsatile flow. *J Biomech Eng* 107: 112–122, 1985.
14. **Langewouters GJ.** *Visco-elasticity of the human aorta in vitro in relation to pressure and age* (PhD thesis). Amsterdam: Free University, 1982, p. 221.
15. **Latham RD, Westerhof N, Sipkema P, Rubal BJ, Reuderink P, Murgo JP.** Regional wave travel and reflections along the human aorta: a study with six simultaneous micromanometric pressures. *Circulation* 72: 1257–1269, 1985.
16. **Luchsinger PC, Snell RE, Patel DJ, Fry DL.** Instantaneous pressure distribution along the human aorta. *Circ Res* 15: 503–510, 1964.
17. **Meister JJ.** *[Doppler ultrasound measurement and theoretical modeling of the effect of heart disease on arterial pressure and flow* (PhD thesis).]. Lausanne: EPFL, 1983, p. IV, 125.
18. **Murgo JP, Westerhof N, Giolma JP, Altobelli SA.** Aortic input impedance in normal man: relationship to pressure wave forms. *Circulation* 62: 105–116, 1980.
19. **Noordergraaf A, Verdouw D, Boom HB.** The use of an analog computer in a circulation model. *Prog Cardiovasc Dis* 5: 419–439, 1963.
20. **Olufsen MS, Peskin CS, Kim WY, Pedersen EM, Nadim A, Larsen J.** Numerical simulation and experimental validation of blood flow in arteries with structured-tree outflow conditions. *Ann Biomed Eng* 28: 1281–1299, 2000.
21. **Papapanayotou CJ, Cherruault Y, Delarochefoucauld B.** A mathematical-model of the Circle of Willis in the presence of an arteriovenous anomaly. *Computers & Mathematics with Applications* 20: 199–206, 1990.
22. **Raines JK, Jaffrin MY, Shapiro AH.** A computer simulation of arterial dynamics in the human leg. *J Biomech* 7: 77–91, 1974.
23. **Reymond P, Merenda F, Perren F, Rufenacht D, Stergiopulos N.** Validation of a one-dimensional model of the systemic arterial tree. *Am J Physiol Heart Circ Physiol* 297: H208–H222, 2009.
24. **Segers P, Rietzschel E, Heireman S, De Buyzere M, Gillebert T, Verdonck P, Van Bortel L.** Carotid tonometry versus synthesized aorta pressure waves for the estimation of central systolic blood pressure and augmentation index. *Am J Hypertens* 18: 1168–1173, 2005.
25. **Stergiopulos N, Young DF, Rogge TR.** Computer simulation of arterial flow with applications to arterial and aortic stenoses. *J Biomech* 25: 1477–1488, 1992.
26. **Stettler JC, Niederer P, Anliker M.** Theoretical analysis of arterial hemodynamics including the influence of bifurcations. Part I: mathematical models and prediction of normal pulse patterns. *Ann Biomed Eng* 9: 145–164, 1981.
27. **Stettler JC, Niederer P, Anliker M, Casty M.** Theoretical analysis of arterial hemodynamics including the influence of bifurcations. Part II: critical evaluation of theoretical model and comparison with noninvasive measurements of flow patterns in normal and pathological cases. *Ann Biomed Eng* 9: 165–175, 1981.
28. **Wan J, Steele B, Spicer SA, Strohband S, Feijoo GR, Hughes TJ, Taylor CA.** A one-dimensional finite element method for simulation-based medical planning for cardiovascular disease. *Comput Methods Biomech Biomed Engin* 5: 195–206, 2002.
29. **Westerhof BE, Guelen I, Stok WJ, Lasance HA, Ascoop CA, Wesseling KH, Westerhof N, Bos WJ, Stergiopulos N, Spaan JA.** Individualization of transfer function in estimation of central aortic pressure from the peripheral pulse is not required in patients at rest. *J Appl Physiol* 105: 1858–1863, 2008.
30. **Westerhof BE, van den Wijngaard JP, Murgo JP, Westerhof N.** Location of a reflection site is elusive: consequences for the calculation of aortic pulse wave velocity. *Hypertension* 52: 478–483, 2008.
31. **Westerhof N, Bosman F, De Vries CJ, Noordergraaf A.** Analog studies of the human systemic arterial tree. *J Biomech* 2: 121–143, 1969.
32. **Zagzoule M, Marc-Vergnes JP.** A global mathematical model of the cerebral circulation in man. *J Biomech* 19: 1015–1022, 1986.